Capillarity

Vol. 18, No. 1, p. 1-13, 2026

Original article

Effect of pore structure on liquid-gas flow in porous media

Zhao Lu[1,2]*, Xiaoxiao Liu[1], Hai Luo[1], Tao Zhang[1], Jie Yang[1], Limin Zhang[1,3]

[1]*Hainan Institute of Zhejiang University, Sanya 572025, P. R. China*

[2]*HKUST Shenzhen-Hong Kong Collaborative Innovation Research Institute, Shenzhen 518000, P. R. China*

[3]*Department of Civil and Environmental Engineering, The Hong Kong University of Science and Technology, Hong Kong 999077, P. R. China*

Keywords:
Pore structure
two-phase flow
uniform porosity
model homogeneity

Cited as:
Lu, Z., Liu, X., Luo, H., Zhang, T., Yang, J., Zhang, L. Effect of pore structure on liquid-gas flow in porous media. Capillarity, 2026, 18(1): 1-13.
https://doi.org/10.46690/capi.2026.01.01

Abstract:
Pore structure significantly governs the seepage characteristics of porous media. This study investigates this influence by comparing the infiltration behavior of homogeneous and heterogeneous porous structures through microfluidic experiments and numerical simulations. It constructed one heterogeneous structure derived from real rock cores and four homogeneous structures with regular particle arrangements, all with identical porosity. Heterogeneous structure and homogeneous structure exhibit similar finger-like flow patterns and minimal differences in water saturation. Air displacement in dead-end pores is driven by internal-external pressure differences, with water replacing air only when internal pressure surpasses external pressure. In homogeneous models, water pressure shows pulse-like fluctuations; pressure peaks due to interfacial resistance decrease from approximately 88 Pa to approximately 38 Pa as pore size increases. Meniscus evolution, linked to pore width variations, presents three states: Stretching, equilibrium, and expansion. This study clarifies the dominant role of pore morphology in fluid transport, providing a theoretical basis for optimizing structural design and efficiently regulating seepage processes in engineering applications such as resource extraction and CO_2 sequestration.

1. Introduction

The infiltration of porous media is a ubiquitous occurrence observed in numerous significant scientific phenomena, spanning industrial production processes and natural environments alike. Examples include groundwater seepage in the soil (Culligan et al., 2000), carbon sequestration (Bachu, 2015), and oil recovery processes (Morrow and Mason, 2001). For an extended period, numerous scholars have conducted extensive research on the seepage characteristics of porous media (Lu et al., 2025a; Zeng et al., 2025). Based on existing research findings, the primary factors influencing the seepage characteristics of porous media include the physical properties of the fluid, porosity, pore connectivity, particle shape, specific surface area, and so forth (Nimmo, 2004; Jiang et al., 2011; Li et al., 2021).

In the existing research on fluid flow in porous media, scholars commonly employ idealized models such as capillary networks or regular arrays of spheres to simulate the structural characteristics of porous media for studying fluid flow (Adler and Thovert, 1998). Alternatively, scholars consider the detailed geometry of a given porous medium, which can be periodically or randomly arranged "particles" of various shapes (Zalc et al., 2003). The porous medium model is constructed by means of the aforementioned method to explore the fluid flow characteristics. Hu et al. (2017a, 2017b) constructed a two-dimensional (2D) microscopic model of round particles with the same size and uniform arrangement.

Yandy Scientific Press

*Corresponding author.
E-mail address: zhao_lu@zju.edu.cn (L. Zhao); xxliu616@zju.edu.cn (X. Liu); luohai@zju.edu.cn (H. Luo); 0917900@zju.edu.cn (T. Zhang); yangjiea@zju.edu.cn (J. Yang); cezhangl@ust.hk (L. Zhang).
2709-2119 © The Author(s) 2025.
Received November 11, 2025; revised December 9, 2025; accepted December 29, 2025; available online January 1, 2026.

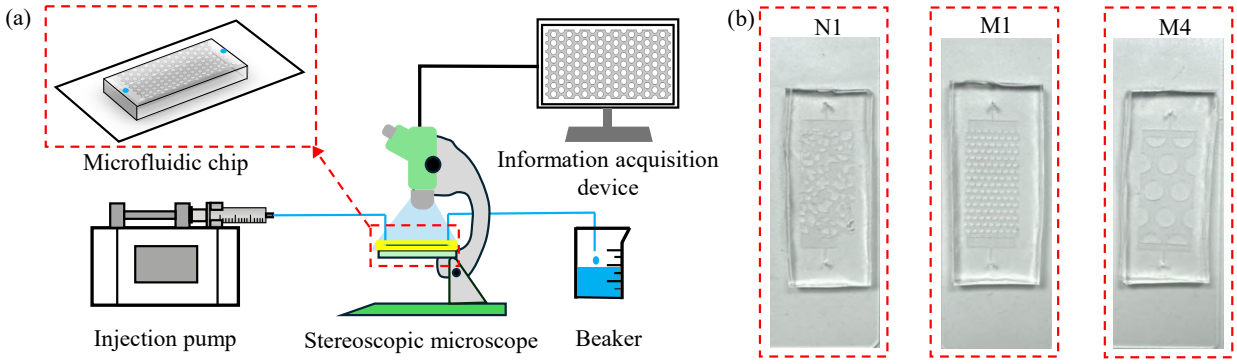

Fig. 1. Microfluidic test device diagram: (a) Schematic diagram of the microfluidic platform and (b) microfluidic chips.

Subsequently, they established a three-dimensional numerical model to validate their findings. The influence of wettability on the immiscible displacement of supercritical CO_2 and brine was investigated, as well as the capillary trapping behavior of supercritical CO_2. Rokhforouz and Akhlaghi Amiri (2017) constructed a heterogeneous porous medium characterized by a circular particle arrangement. Their study focused on the countercurrent imbibition process and examined the impact of factors such as interfacial tension. Using a 2D Vronoi diagram, Yong et al. (2014) established a porous media model with randomly connected large pore channels, simulated the heterogeneity of porous media, and investigated the effect of the pore structure on the diffusion process of porous media. Nevertheless, when juxtaposed with actual porous media, idealized models tend to be simpler, making it challenging to characterize the structural intricacies inherent in complex real porous media.

In previous studies, idealized models have been predominantly utilized as the primary research focus due to the inherent difficulty in observing fluid flow processes and phase distribution within real porous media. However, with advancements in technology, it is becoming increasingly convenient to sample actual pore structures. X-ray computed tomography (CT) offers a precise means of characterizing porous structure and geometry. Relevant scholars have also conducted a large number of experimental studies (Rücker et al., 2019; Soltanmohammadi et al., 2021, 2024). However, this method is often expensive. In contrast, the rapid development of microfluidic technology provides a new research direction for the study of pore scale fluid flow. Through etching the designed porous network onto the microfluidic chip, microfluidic technology enables a more intuitive visual analysis of fluid flow. This capability offers significant convenience for investigating fluid flow in porous media. Holtzman and Segre (2015) constructed a porous media model characterized by an equilateral triangle geometry arrangement, achieved by introducing disorder into the random variation process of circular particle size. They conducted microfluidic experiments and numerical simulations to elucidate the combined impacts of wettability and dynamics on immiscible displacement in disordered media. Zhan et al. (2021) and Li et al. (2022, 2023) investigated the physical behavior of the capillary barrier effect in the microscopic state by etching the geometric structure forms of square and honeycomb arrangements in microfluidic chips. Nevertheless, the aforementioned scholars continued to employ artificially constructed idealized models to investigate the fluid flow process. Therefore, it is feasible to explore the structural characteristics of porous media by etching the real pore structure in microfluidic chips (Lu et al., 2025b).

The goal of this study was to evaluate the effect of porous media homogeneity on the infiltration effect. Three types of microfluidic chips were fabricated by microfluidic technology with the identical porosity, including heterogeneous structure N1 and homogeneous structure M1 and M4. N1 is derived from 2D slices of real rock and can characterize complex porous media structures. M1and M4 are composed of staggered arrangements of circular micropillars. In addition, five numerical simulation models based on the microfluidic chips was developed to validate the accuracy. Furthermore, two simulation models M3 and M4 are added based on this foundation. The homogeneous model that can describe the heterogeneous model N1 were explored by analyzing the evolution of water shape, water saturation, and pressure variations during the infiltration process.

2. Microfluidic experiments

2.1 Experimental set-up

The microfluidics platform used in the present study comprised four components: An injection system, microfluidic chips, a stereoscopic microscope and an information acquisition device. The microfluidic injection system consisted of an injection pump (PHD2000, Harvard Apparatus, US) and a polypropylene syringe. The injection pump could provide an injection rate of 0.0033 μL/min to 205.30 ml/h. As shown in Fig. 1(a), the microfluidic injection pump injected water into the microfluidic chip at a constant flow rate. The stereoscopic microscope (T2-3M180, Aosvi, z) was connected to the information acquisition device. A camera with image and video capture functions was installed in the microscope, and the stored data could be uploaded to the information acquisition device for display. This study fabricated three distinct microfluidic chips with diverse internal pore structure, including two homogeneous pore structures, M1 and M4, characterized by an orderly arrangement of circular particles, as well as a heterogeneous pore structure, N1, derived from the

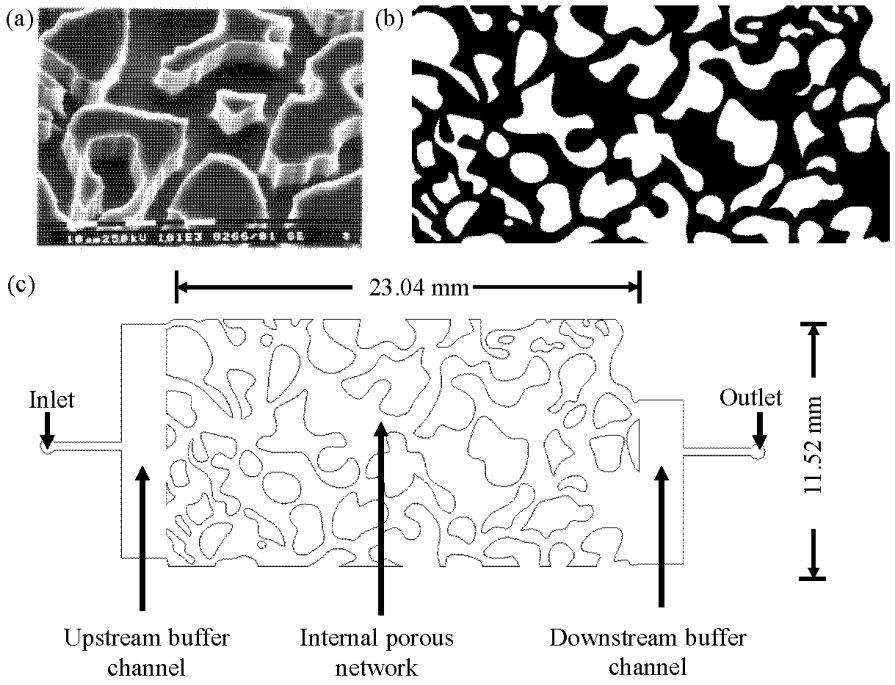

Fig. 2. Introduction of heterogeneous pore structure N1: (a) SEM images of etched patterns on silicon wafers (Sirivithayapakorn and Keller, 2003), (b) Diagram of heterogeneous pore structure and (c) Designed pore structure in the microfluidic chip.

pore evolution of a real rock core. The microfluidic chip was fabricated from a transparent material with high transmittance, specifically polydimethylsiloxane, as depicted in Fig. 1(b).

The homogeneous pore structures M1 and M4 exhibit identical particle arrangement patterns but differ in pore throat size and particle dimensions, specifically engineered to elucidate the influence of pore throat width on infiltration front morphology. The internal structural dimensions will be detailed in Section 3. The heterogeneous pore structure N1 was engineered based on pore-scale flow experiments conducted by Arturo Keller's team (Sirivithayapakorn and Keller, 2003), which utilized serial sectioning technology to dissect natural sandstone samples, coupled with scanning electron microscopy (SEM) to perform reconstruction of intra-core pore networks with sub-micron resolution. Subsequently, the geometric pattern obtained from these analyses was transferred onto a silicon wafer via etching techniques to fabricate a 2D pore structure model, as illustrated in Fig. 2(a). Furthermore, image binarization were applied to transform the SEM images into 2D digital models in DXF format, thereby generating the pore structure schematic diagram presented in Fig. 2(b). This digital model accurately preserves the fractal characteristics and spatial heterogeneity of the pore-throat system in natural rocks, thus providing a physical foundation for investigating the migration patterns of multiphase flow under the constraints of complex pore geometries. In this study, based on the digital model, the functional design of the microfluidic chip was accomplished through CAD software. While preserving the geometric integrity of the original pore structure, inlet, outlet and buffer layers were incorporated into the two lateral regions of the model, as depicted in Fig. 2(c), thereby establishing an experimentally feasible microfluidic chip structural design scheme.

The homogeneous pore structures maintain identical porosity and external dimensions to the heterogeneous structure, differing solely in their internal structure. The interior of the chip was etched with various pore structure configurations to mimic the structure of porous media. All three chips shared the same total patterned network area, measuring 23.04×11.52 mm^2. Each microfluidic chip contained an inlet, upstream buffer channel, internal porous network, downstream buffer channel and an outlet, as shown in Fig. 2(c). The inlet was connected with the polypropylene syringe and the outlet was connected with the beaker. When water in the polypropylene syringe was injected into the chip using the injection pump, it initially filled the buffer channel and then distributed the flow uniformly. The entire testing process was conducted at room temperature, approximately 20 °C.

2.2 Test procedure

The experiments entailed injecting deionized water at a constant rate into a dry microfluidic chip until the water-air front reached the outlet. The full process of water migration during the injection phase was recorded via a microscope, with the collected data thereafter transferred to the information acquisition device. Before the experiment commenced, the microfluidic chip was rinsed by pumping deionized water at a flow rate of 500 μL/min for 2 minutes, followed by thorough drying at 85 °C for 2 hours. Post-drying, the chip was kept at ambient laboratory temperature for 2 hours to achieve thermal equilibrium. Afterwards, the experimental setup was assembled as required, and the test was initiated, as shown in Fig. 1(a). The microfluidic injection pump was

configured to inject water into the chip at a flow rate of 10 mL/min, corresponding to a Darcy's velocity within the chips of 3×10^{-4} m/s. The microscope captured photos and recorded in real-time until the water-air interface reached the exit and stabilized, signifying the completion of the experiment.

3. Numerical simulation

In this section, the governing equations, model geometry, boundary condition setting and model meshing are presented. All the simulation models in the present study were conducted using the phase field method in the COMSOL Multiphysics software. In addition, based on microfluidic experiments, two homogeneous models M2 and M3 are added in this section to investigate the homogeneous model that can best represent heterogeneous porous media.

3.1 Governing equations

The Cahn-Hilliard phase-field method (Cahn and Hilliard, 1958) coupled with Navier-Stokes and continuity equations was used to solve the interface problem of two-phase fluid flow.

The modified Navier-Stokes and continuity equations were coupled with the phase-field equation to capture the moving interface. Navier-Stokes equations are primarily used to describe changes in the mass and momentum of a fluid. The interfacial tension was introduced into the Navier-Stokes equation as a mass force to describe the flow of a two-phase fluid. Cahn-Hilliard equation was used to explain the phase separation process. The equations are as follows (Jacqmin, 1999; Badalassi et al., 2003):

$$\rho\frac{\partial u}{\partial t}+\rho(u\cdot\nabla)u=\nabla\left[-p+\mu\left(\nabla u+(\nabla u)^{T}\right)\right]+F_{st}+F_{g} \quad (1)$$

$$\nabla\cdot u=0 \quad (2)$$

$$\frac{\partial\phi}{\partial t}+u\cdot\nabla\phi=\nabla\frac{\gamma\lambda}{\varepsilon^{2}}\nabla\psi \quad (3)$$

$$\psi=-\nabla\cdot\varepsilon^{2}\nabla\phi+(\phi^{2}-1)\phi+\left(\frac{\varepsilon^{2}}{\lambda}\right)\frac{\partial f_{ext}}{\partial\phi} \quad (4)$$

where u denotes the fluid velocity, t denotes time, ρ is the fluid density, p is the pressure, T is temperature, γ is the mobility, λ is the mixing energy density, ε is the capillary width, ψ is the phase field help variable, ϕ is the phase-field order parameter, f_{ext} is the external free energy density, and F_g and F_{st} are the gravity and interfacial tension acting on the fluid interface.

Navier-Stokes and Cahn-Hilliard are solved simultaneously with the continuity equation, which is as follows (Amiri and Hamouda, 2014):

$$\frac{\partial\rho}{\partial t}+\nabla\cdot(\rho u)=0 \quad (5)$$

In the phase field method, the dynamic viscosity (μ) and density (ρ) of mixing fluid are defined according to the density (ρ_1, ρ_2) and dynamic viscosity (μ_1, μ_2) of two fluids, the gravity force (F_g) and surface tension (F_{st}) can be expressed as (Qin and Bhadeshia, 2010):

$$\rho=(1-V_{f2})\rho_1+(V_{f2})\rho_2 \quad (6)$$

$$\mu=(1-V_{f2})\mu_1+(V_{f2})\mu_2 \quad (7)$$

$$F_g=\rho g \quad (8)$$

$$F_{st}=\left(G-\frac{\partial f_{ext}}{\partial\phi}\right)\nabla\phi \quad (9)$$

where the subscripts 1 and 2 denote the wetting phase and non-wetting phase, respectively; g is the gravitational acceleration, G is the chemical potential.

V_{f2} is the volume fraction of fluid 2, which is defined as (Amiri and Hamouda, 2014):

$$V_{f2}=\frac{1+\phi}{2} \quad (10)$$

$$0\le V_{f2}\le 1 \quad (11)$$

After introducing Eq. (10) into Eqs. (7) and (8), the equal regarding the fluid properties with respect to the phase field auxiliary variable can be derived:

$$\vartheta(\phi)=\frac{(1+\phi)}{2}\vartheta_1+\frac{(1-\phi)}{2}\vartheta_2 \quad (12)$$

where ϑ represents each phase property such as viscosity (μ) and density (ρ).

The fundamental concept of the phase-field method lies in the introduction of a continuous field variable, namely the phase-field order parameter ϕ. This approach assumes that the interface between phases is diffusive, and the diffuse interface between two phases is expressed using a continuous interpolation function based on the phase-field variable ϕ. Consequently, this avoids the computational complexity associated with directly tracking the interface in traditional methods (Takada et al., 2005). Fig. 3 presents schematic representations of the diffuse interface in the phase-field method and the sharp interface inherent to the traditional method. The phase-field order parameter (ϕ) is defined such that the relative concentrations of the two phases are $(1+\phi)/2$ and $(1-\phi)/2$. In this definition, $\phi=1$ represents fluid 1, and $\phi=-1$ represents fluid 2 that is not miscible with fluid 1. The transition area representing the two-phase interface is denotes as 2ε. The set of values of the order parameter over the whole volume is the phase field (Qin and Bhadeshia, 2010). The physical properties of all fluids were interpolated between the two phases using the relative concentration of the phases, as expressed in Eq. (12).

In Eq. (9), κ is defined in terms of mixing energy density (λ) and capillary width (ε) as:

$$G=\lambda\left[-\nabla^{2}\phi+\frac{\phi(\phi-1)}{\varepsilon^{2}}\right]+\frac{\partial f_{ext}}{\partial\phi} \quad (13)$$

The surface tension coefficient for the phase-field model is equal to the integral of the free energy density across the interface. The relationship between the mixed energy density (λ), the capillary width (ε) and the surface tension (σ) is:

$$\sigma=\frac{2\sqrt{2}}{3}\frac{\lambda}{\varepsilon} \quad (14)$$

The relationship between the mobility (γ), the capillary width (ε) and the mobility tuning parameter (χ) is as follows (Hizir and Hardt, 2014):

$$\chi=\frac{\gamma}{\varepsilon^{2}} \quad (15)$$

The parameter χ is introduced by COMSOL to control the

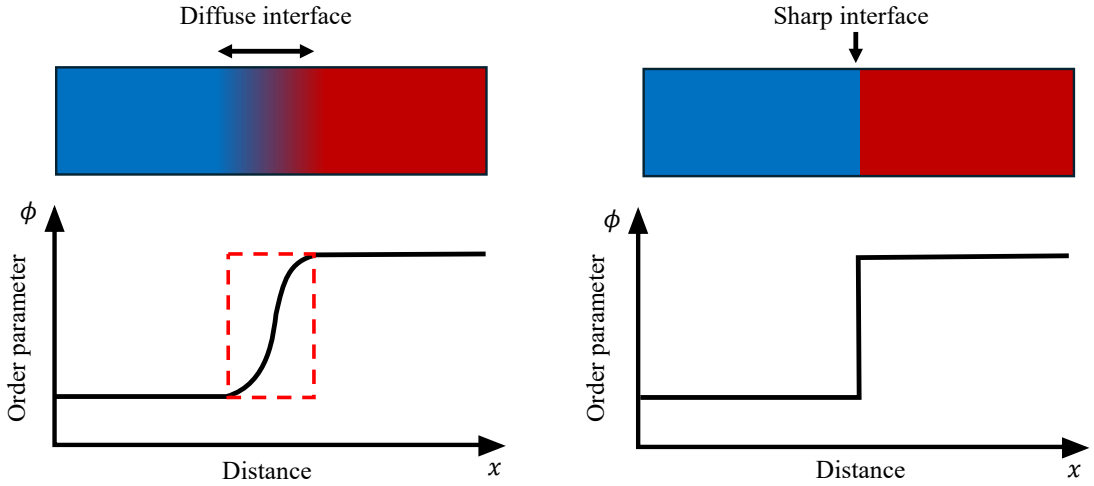

Fig. 3. Schematic of diffuse interface and sharp interface.

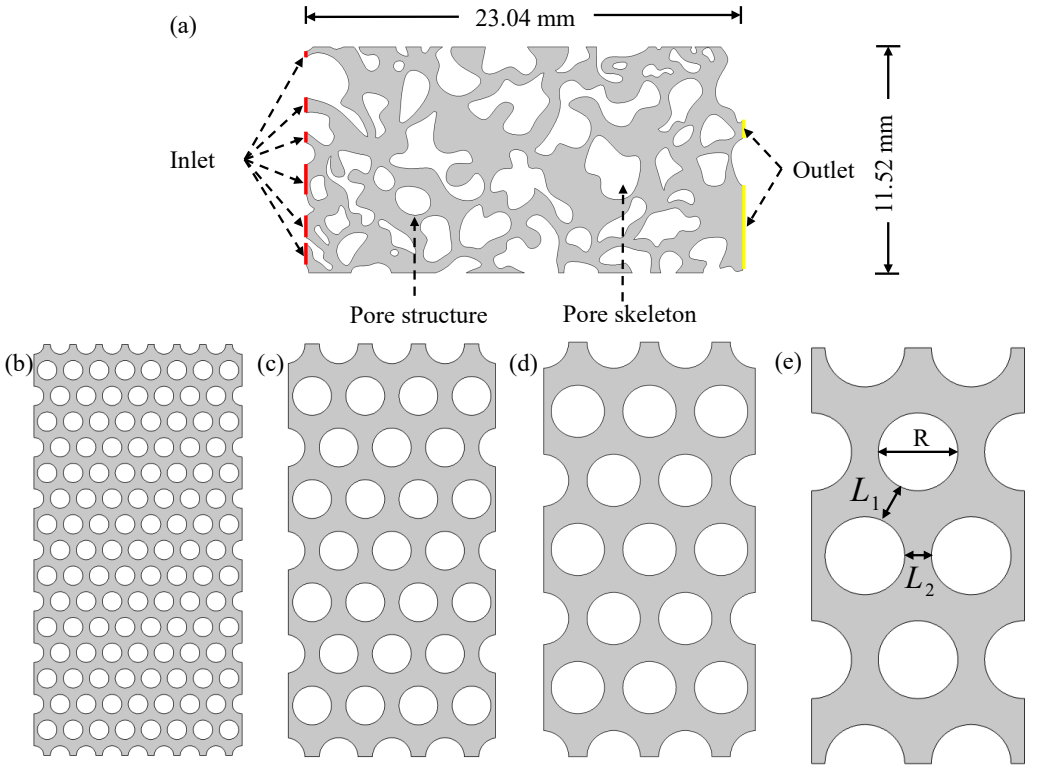

Fig. 4. Schematic diagram of the microstructure models: (a) N1, (b) M1, (c) M2, (d) M3, and (e) M4.

diffusion-related time scale for the interface.

3.2 Model geometry and boundary conditions

The geometry of the simulated domain, which mirrors the internal pore structure of the microfluidic chips, is illustrated in Fig. 4; the domain has dimensions of 11.52 mm × 23.04 mm, and all models share a consistent porosity of 0.553. N1 represents the heterogeneous porous media model, incorporating a complex pore structure derived from 2D slices of real rock. M1, M2, M3 and M4 were homogeneous porous media models, wherein the matrix blocks were represented by an isosceles triangular array of circles. In Fig. 4, the white area symbolizes the porous media matrix, while the gray area depicts the pore structure. Geometrical dimensions of different numerical models were present in Table 1.

The simulation assumed that each phase was incompressible and that phase change did not occur. Gravity was neglected by assuming 2D horizontal flow. Initially, the porous medium was filled with air. Water was injected with a constant velocity of 3.3×10^{-4} m/s from the inlet, and the outlet pressure was set to zero. All other boundaries of the model were assigned no-slip boundary conditions. Additionally, the boundary condition of internal surfaces was set as a wetted wall with a specified contact angle.

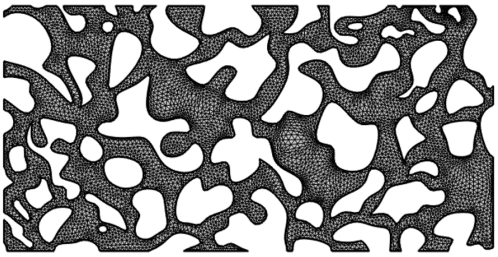

Fig. 5. Mesh division diagram of N1.

Table 1. Geometrical dimensions of different numerical models considered in present work.

Model	Porosity ε	Particle diameter R (mm)	Inclined spacing L_1 (mm)	Horizontal spacing L_2 (mm)	Inlet velocity v (m/s)
N1		/	/	/	
M1		1.08	0.53	0.36	
M2	0.553	2.16	1.08	0.80	3×10^{-4}
M3		2.90	1.41	1.00	
M4		4.32	2.12	1.44	

3.3 Meshing

The accuracy of the solution outcomes was significantly influenced by the level of mesh refinement. Finer meshes yielded solutions closer to reality. In the present study, an unstructured free triangle mesh with a size of 0.2 mm was employed for mesh division. The meshes were calibrated using fluid dynamics. The numbers of meshes used in the N1 and M1-M4 models were 15,468, 23,484, 16,066, 13,489 and 16,307, respectively. The mesh division diagram of heterogeneous model N1 is shown in Fig. 5.

4. Results

4.1 Evolution of water morphology

To investigate the evolution process of water morphology at different moments, a comparison of water morphology was obtained from both experimental testing and simulation at various representative moments within the heterogeneous porous media N1 (Fig. 6). The normalized length λ of the water front was used to characterize the water morphology (Hu et al., 2017a, 2017b). Here, L is the distance from the water front tip to the inlet boundary of the porous network, and L_{total} is the total length of the porous network along the flow direction. As demonstrated in Fig. 6, there is a strong agreement between the test results and numerical simulation results, with consistent overall infiltration trends observed. During the initial stage, infiltration predominantly occurred along the channel with a wider pore in the middle, as shown in Fig. 6 with $\lambda = 0.21$. At this moment, there were three main flow directions of water (blue arrow in Fig. 6). The first direction exhibited flow towards the lower right, with the water-air interface smoothly traversing a narrow channel towards the rear macropore. The second direction involved horizontal infiltration towards the right. In the third direction, flow proceeded along the lower left. Further, among the three seepage channels in the early stage of infiltration, only the test of channel 1 was highly consistent with the numerical results. In the rear macropore, water accumulation occurred, eventually leading to blockage at the narrower pore. This process resulted in the formation of typical finger-like flow patterns, with the finger length surpassing the finger width. However, disparities were noted between the test and numerical results for channels 2 and 3. In the experimental findings, water in channel 2 halted before reaching the right-side wall, leaving a larger area of residual gas trapped beneath under the clamp of the water in channel 1. Conversely, in the numerical simulation results, water failed to infiltrate into channel 3 altogether. In the subsequent seepage process, the infiltration results from both the test and numerical simulation exhibit a basic consistency, with only minor differences observed. This discrepancy may stem from errors in the fabrication process of the microfluidic chip, such as the roughness of the pore surface. As numerical simulation represents an idealized model, disparities between the test and simulation results are expected. Upon completion of displacement, examination of the two-phase distribution diagram at a stable time reveals that residual gas was predominantly distributed in the dead-end pores.

A comparison of water morphology obtained from both experimental testing and simulation at various representative moments in the homogeneous porous media M1 and M4 is presented in Fig. 7. Within homogeneous porous medium M1, water advanced with a relatively compacted morphology during the infiltration process. The more stable water front diminishes the likelihood of air trapping. As such, finger-like flow failed to manifest in this scenario. Owing to the dense arrangement of particle structures, water encountered significant capillary resistance during infiltration. As the water front tip percolated from one row of pores to the next, it would be impeded until all water-air interfaces aligned horizontally. Subsequently, infiltration would resume downward. The phenomenon of water passing in a row during infiltration, known as the “queuing effect”, was observed. This effect not only hampered finger-like flow but also significantly enhanced water saturation in porous media. A comparison between the test and simulation results of M1 reveals that only a portion of residual gas was generated on both sides of the wall during the test. Meanwhile, in the simulation, it was observed at the exit position. Further, the area of residual gas formed was considerably small, almost negligible. In the homogeneous porous medium M4, which featured wider pores and fewer infiltration channels, the water-gas interface was relatively flat during the initial stage of infiltration. However, a significant area of residual gas remained at the entrance. Yet, in the middle and late stages of infiltration, the water morphology changed. At $\lambda = 0.60$, residual gas was observed when the water-gas interface breached the middle pore and converged with the water-air interface on both the left and right sides. When $\lambda = 0.84$, water began flowing out of the left channel and, following breakthrough, rapidly flowed toward the exit.

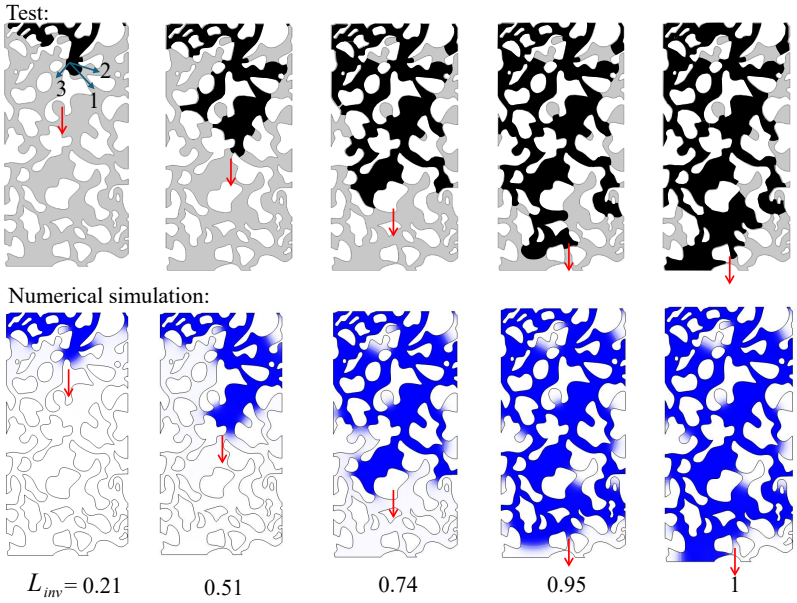

Fig. 6. Comparison of water morphology obtained from test and simulation in N1.

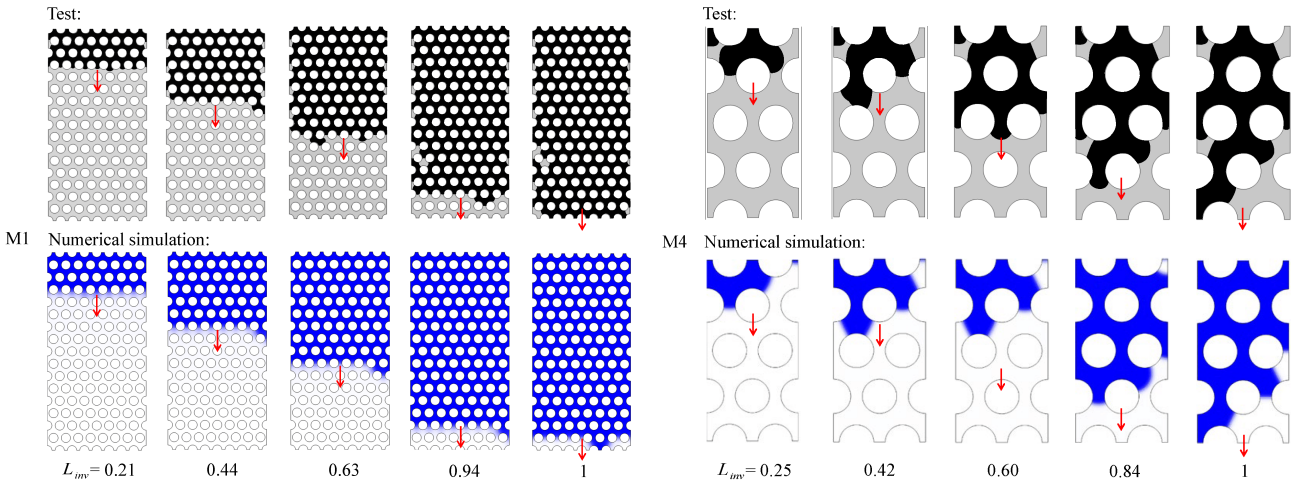

Fig. 7. Comparison of water morphology obtained from M1 and M4.

Subsequently, the water flow tended to stabilize. Similar to the heterogeneous porous medium N1, finger-like flow emerged during the water flow process, accompanied by a significant area of residual gas. However, the difference lies in the presence of dead-end pores in N1, resulting in a relatively dispersed distribution of residual gas, with each region's area not being substantial.

In summary, the homogeneity of porous media manifested a noticeable difference in the evolution of water morphology during infiltration. In heterogeneous porous media, water tended to pass through the wider seepage channels initially, resulting in the formation of finger-like flow patterns with a much greater length than width. Eventually, water diffused from these channels. For the homogeneous model with small pore structures, water tends to form a flatter water-air interface during infiltration, thereby reducing the likelihood of air trapping. In contrast, for the homogeneous model with larger pores, the internal seepage channels are fewer, resulting in a relatively stable water-air interface during the initial stage of infiltration. However, a significant area of air was still trapped within the medium. Moreover, with the injection of water, the stability of the interface gradually decreased, and eventually a wider finger-like flow was formed.

4.2 The changes in water saturation

To assess the influence of porous media homogeneity on water saturation, the water saturation of simulation results at a stable moment for the five porous media are depicted in Fig. 8(a). It is evident that the water saturation in N1 fell between that of M3 and M4 under constant inlet flow rate conditions. In the simulation results, the saturation of N1 stabilized at around 0.85, whereas the saturation levels of M1, M2, M3 and M4 were 0.95, 0.91, 0.89 and 0.82, respectively. Among them, the difference of the water saturation between N1 and

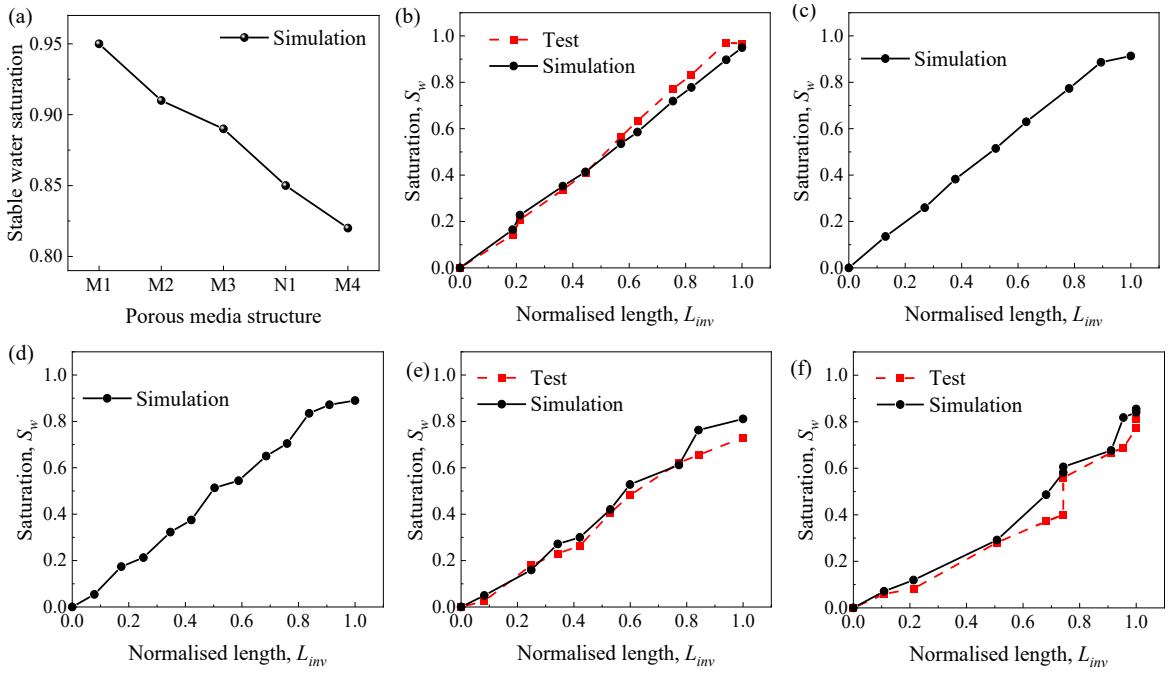

Fig. 8. Evolutions of the water saturation during water flow processes: (a) Stable water saturation, (b) M1, (c) M2, (d) M3, (e) M4, and (f) N1.

M4 was small. Therefore, in terms of water saturation, the results for M4 and N1 show better agreement. However, it is not sufficient to judge the similarity of the models solely based on the final water saturation results. In order to further analyze the discrepancies among the models, the curves of internal saturation of porous media with normalized length λ for each model are presented below.

The evolutions of the water saturation S_w with normalized length λ during the flow processes were plotted, as shown in Figs. 8(b)-8(f). Among them, M2 and M3 were only investigated through numerical simulation, whereas the remaining three groups were validated through microfluidic tests. The test results were found to be in better agreement with the results of the simulations. An observation can be made from Figs. 8(b) and 8(c) that the saturation curve of M1 and M2 basically maintained a linear increase. The queuing effect is responsible for this phenomenon. The consistent progression of the water-air interface minimizes residual gas formation, leading to a gradual stable saturation curve ascent and higher water saturation. Nonetheless, the saturation curve of M3 and M4 experiences significant fluctuations. From the perspective of fluctuation, M3 exhibits a more regular curve compared to M4, which resembles the steady ascent of a ladder. Because of its wide spacing between adjacent rows of particles, requiring a significant volume of water for complete filling the area. Consequently, there is a rapid increase in the saturation curve over the same length of infiltration. Furthermore, as a result of the queuing effect, water will encounter higher capillary resistance before infiltrating the next layer of particles, leading to a slower increase in the saturation curve. Therefore, the saturation curve of M3 eventually exhibits resembles the steady ascent of a ladder. Nonetheless, the saturation curve of the homogeneous porous medium M4 experiences significant fluctuations. Because of its loose pore structure, the water-air interface suffered less capillary resistance during infiltration, and the queuing effect is not obvious. Moreover, the water flow would percolate around the particles upon coming into contact with them. And the width of the pore throat at the boundary was smaller than the width between adjacent particles, resulting in a speed discrepancy as water passed through. As such, a significant area of residual gas formed at the boundary, influencing the curve's evolution.

The intricate structure of heterogeneous porous media resulted in significant disorder in the distribution of percolation channels and variations in pore size. As shown in Fig. 8(d), the saturation curve fluctuated sharply. When water infiltrates heterogeneous porous media, it tends to preferentially flow along single seepage channels characterized by larger pore throats and lower capillary resistance. An observation can be made from the simulation results that in the initial stage of infiltration ($L_{inv} < 0.5$), the change in water saturation was relatively small, and was basically consistent with the test results. When $L_{inv} > 0.5$, the water saturation notably increased. When the normalized length exceeds 0.5, water saturation increases notably. At this stage, the water-air interface encounters obstruction at narrow positions in the seepage channel; water spreads around the channel, leading to an overall increase in water saturation. For example, when the normalized length increases from 0.51 to 0.68 (an increase of 0.17), saturation rises by approximately 20%; when the normalized length increases from 0.68 to 0.74 (an increase of 0.06), saturation rises by approximately 10%. The two-phase interface distributions of three points between $L_{inv} = 0.51$-0.74 in the simulation results were selected respectively, as shown

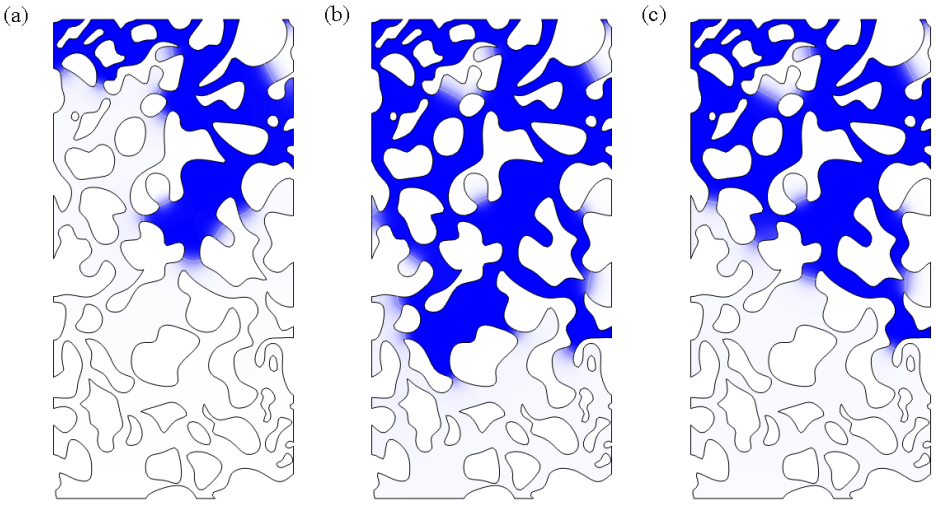

Fig. 9. Numerical results of two-phase distribution between $L_{inv} = 0.51$-0.74: (a) 0.51, (b) 0.68 and (c) 0.74.

in Fig. 9. As can be seen from Fig. 9(a), when $L_{inv} = 0.51$, there was still a large area of air distribution under the porous medium. Although the water-air front was longer at this time, the saturation was lower. When $L_{inv} = 0.68$, as shown in Fig. 9(b), the water-gas interface stopped flowing downward at the narrow upper pore, but most of the air under the porous medium was displaced by water. At this time, although L_{inv} only increased by 0.17, the saturation increased by about 20%. As shown in Fig. 9(c), when $L_{inv} = 0.74$, the water in the upper side channel remained stationary, while flow occurred within the middle macropore, resulting in the forward movement of the water-air interface. L_{inv} only increased by 0.06, but the saturation increased by about 10%. Therefore, L_{inv} did not always increase. When the water-air front was blocked, the water-gas interface would flow in another pore with less resistance, resulting in significant fluctuation of saturation with normalized length L_{inv}.

In conclusion, the saturation and water morphology evolution of M4 and N1 were relatively close. Based on the saturation results from numerical simulation, the disparity between M4 and N1 is a mere 0.03. During the infiltration process, both of them exhibited distinct fingered flow, leading to significant fluctuations in the saturation curve. Contrastingly, in M1, M2 and M3 characterized by tight particle arrangement, the water-air interface exhibited uniform advancement throughout infiltration. Consequently, the water saturation of them exhibits a linear growth as L_{inv} increases.

5. Analysis and discussion

5.1 Displacement in dead-end pore

When water flowed through dead-end pores, the water-air interface could cause extrusion of air within the pore. As such, the exchange process between water and gas remained incomplete within dead-end pores, leading to reduced water saturation in the porous medium. However, some dead-end pores may undergo complete displacement of air. To explore the water and air exchange process within dead-end pores, two dead-end pores were selected for analysis, namely one with residual gas and one without. The positions of these dead-end pores are depicted in Fig. 10(a).

To analyze the differences between the two dead pores more intuitively, three points (A, B, and C) were selected in each of the two pores, and the corresponding pressure change diagrams were plotted. These pressure change curves are shown in Figs. 10(b) and 10(c). An observation can be made from Fig. 10(b) that the pressure of hole 1 first reached the peak at about 1.2 s. At this time, the pressure magnitudes of three points can be denoted as follows: A > B > C. This occurrence is attributed to the water-air interface advancing to hole 1 at 1.2 s, exerting pressure on the air within the pore. As water continued to flow, an equilibrium state was established on both sides of the water-air interface, resulting in the pressure inside the pore consistently being lower than the pressure outside. Eventually, residual gas accumulated and sealed within the dead-end pore. However, after pore 2 reached its peak at 2.5 s, the pressure at point A was always greater than that at point C, as shown in Fig. 10(c). Due to the pressure difference, the air inside pore 2 was gradually displaced by water, but this was a slow process. When $t < 5$ s, the internal and external pressure difference of pore 2 was small, the water-air interface slowly pushed into the pore, and the air was difficult to be squeezed out. When $t > 5$ s, a notable increase in pressure was observed at point A, along with an augmented pressure difference. This surge in pressure prompted rapid expulsion of air from within the pore. Around the 5th second, water flowed outside the pore stabilized, causing the pressure at point A to plateau. However, the water-air interface continued to compress air, resulting in increased pore pressure. Consequently, the water-air exchange process within the dead-end pore was primarily driven by pressure differentials. When the pressure inside the pore surpassed that outside, water displaced gas within the pore. In contrast, if the pressure inside the pore was lower, the water-air interface sealed the dead-end pore, impeding gas displacement.

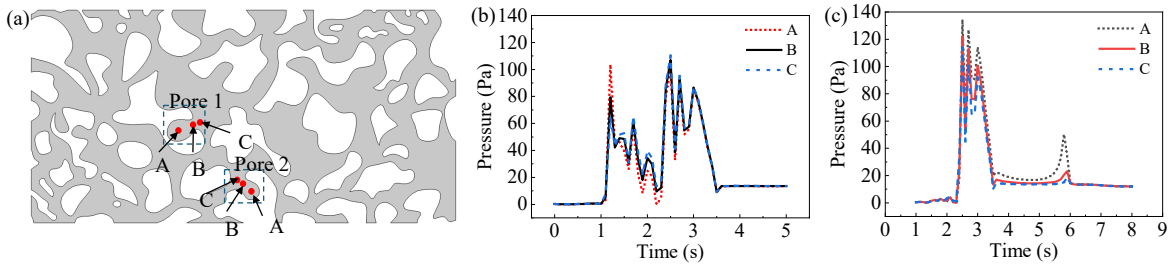

Fig. 10. The position of the selected dead-end pores and corresponding pressure pattern: (a) The distribution and position of dead-end pores, (b) the pressure variation of Pore 1 (residual gas trapped), and (c) the pressure variation of Pore 2 (complete displacement).

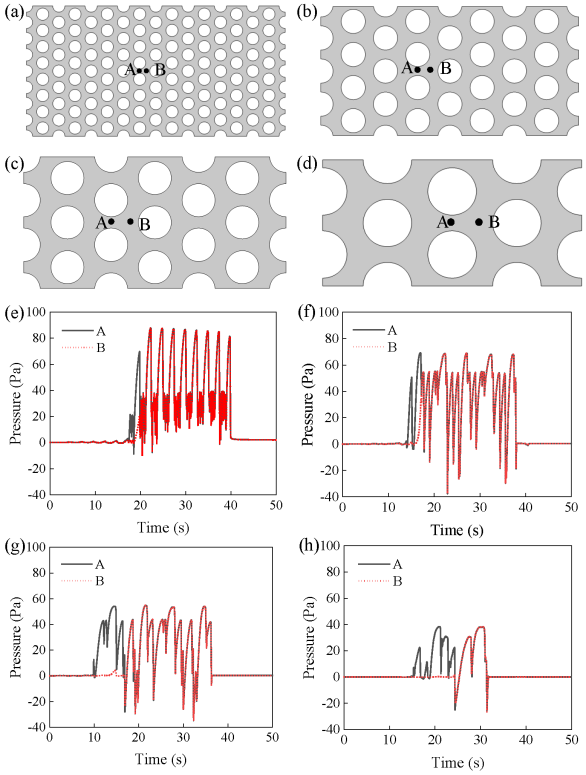

Fig. 11. The analysis of key locations and distributions points (A and B) in porous media models: (a)-(d) Four locations of Point A and B, (e)-(h) are four pressure development of two points A and B.

5.2 Pressure changes in the homogeneous model

The queuing effect is a result of the obstruction of capillary force, and the magnitude of capillary resistance is correlated with the size of pores. To examine the variation of water pressure in porous media during the seepage process, pressure change diagrams over time were plotted for points A and B located between three adjacent particles. Among them, point A is located at the midpoint between the two particles, while point B is situated on the same horizontal axis. The locations of points A and B were depicted in Figs. 11(a)-11(d).

The time-dependent pressure variation curves at Points A and B across the four models are presented in Figs. 11(e)-11(h). It is noteworthy that the pressure evolution over time in all four models displayed a pulse-like fluctuation pattern. Specifically, the peak pressure values decrease with the enlargement of pore sizes. During the infiltration process, the peak pressures measured for Models M1 to M4 were 87.63, 68.68, 54.88, and 38.26 Pa, respectively. In addition, the pressure curves are fluctuated according to a same waveform cycle until the seepage reaches a state of stability. Each waveform consists of a primary peak and multiple secondary peaks. The following four pressure curves each exhibit a cycle period of approximately 2.5, 4.9, 6.5, and 9.5 s respectively. The smaller pore size associated with the shorter the duration of a single wave and the higher the pressure peak. Furthermore, the fluctuation frequency of each waveform was correlated with the number of particle rows behind Points A and B. To explore this correlation, M3 was selected as a representative case, and the time points corresponding to individual wave peaks were identified, as illustrated in Fig. 11.

The two-phase interface diagram corresponding to the time of the peak of the pressure curve at Point B in M3 is shown in Fig. 12(a). As observed, the pressure at Point B achieved its initial peak P_1 at $t = 21.6$ s, which coincides with the water-gas interface within the pores forming a straight line and being on the cusp of breakthrough. After the breakthrough occurs, the pressure declines rapidly, and a subsequent peak P_2 is attained at $t = 27.1$ s. With such cyclic fluctuations, eventually reaches a state of stability following the final peak P_3 at $t = 34.7$ s. From the two-phase interface distribution diagrams corresponding to the three main peaks, it is evident that the water-air interface associated with each pressure peak at Point B emerged at the moment just prior to breakthrough. The queuing effect arose as a result of the substantial resistance encountered by the water-air interface during its penetration through the pores. The water will oppose the capillary force until the middle layer between two adjacent particles was saturated, leading to pressure accumulation. Throughout this process, the pressure would escalate quickly. After the breakthrough, capillary resistance ceases to have an influence, and only air resistance remains unable to stop the flow of water. This leads to a higher flow rate through the pores, worsening the rapid release of water pressure. As a consequence, the pressure will rapidly decrease after the breakthrough. Until the next middle layer becomes saturated with water, initiating the subsequent round of pressure accumulation process.

Notably, there are multiple secondary peaks between two

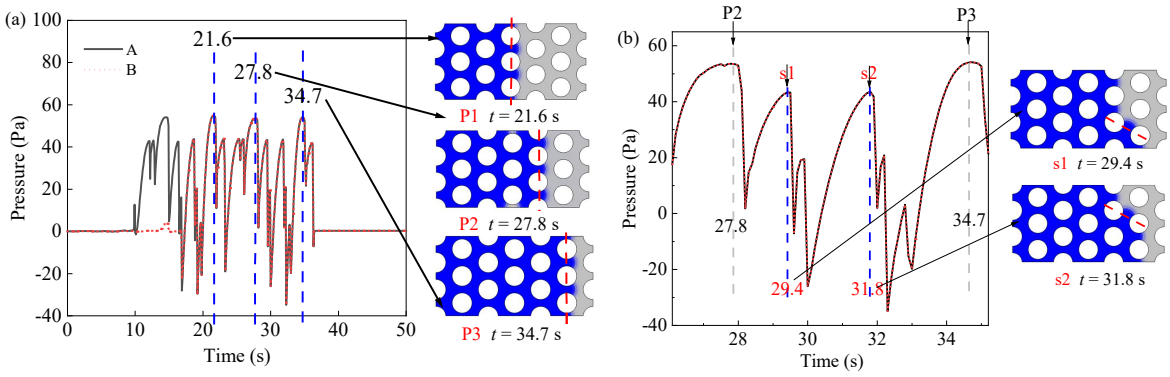

Fig. 12. The two-phase interface analysis of corresponding peak during infiltration in model M3: (a) The primary peak pattern and (b) the secondary pattern.

adjacent primary peaks, as shown from Fig. 12(b). To elucidate the formation of the secondary peaks, an enlarged view of the middle region between the primary peaks P_2 and P_3 is presented in Fig. 12(b), along with a two-phase volume distribution map corresponding to the time of occurrence of the secondary peaks s_1 and s_2. As depicted in Fig. 12(b), at these two time points, the menisci between the two staggered pellets is approaching breakthrough. After the menisci is breached, there will be a rapid decrease in pressure, followed by an accumulation of pressure for breaking through the next menisci. Therefore, the formation of the pressure secondary peak is primarily attributed to the expansion and rupture of the menisci.

As mentioned above, the formation of the primary and secondary pressure peaks is attributed to the expansion of the menisci between the pores, leading to pressure accumulation. After the meniscus is breakthrough, interface resistance ceases to have an influence, and only air resistance remains unable to stop the flow of water, worsening the rapid release of water pressure.

5.3 Evolution of menisci morphology during seepage

During infiltration, the evolution of meniscus shape was influenced by changes in pore width. As the meniscus traversed from a wide to a narrow channel, it underwent arc-shaped contraction, driven by surface tension, which encouraged water flow into the narrow pore. Conversely, when the meniscus transitioned from a narrow to a wide channel, it underwent arc-shaped expansion. In this scenario, water flow had to overcome surface tension.

To further illustrate the meniscus behavior, the motion process and corresponding pressure diagram of the meniscus in M4 and N1 are shown in Fig. 13. The flow direction is from left to right. As shown in Fig. 13(a), the arc length of the meniscus gradually decreased as it moved forward. At this moment, the water pressure was negative, while the air pressure was positive, signifying that water flow was primarily governed by interfacial tension. The relatively low velocity of water instead hindered contraction of the meniscus forward, generating negative pressure on the water side. The negative pressure difference was approximately 26.7 Pa. As the meniscus shrunk, the interfacial tension gradually decreased. An observation can be made from Fig. 13(b) that the meniscus became a straight line at this time, with the pressure contour indicating a negligible pressure difference between the two sides of the interface, signifying equilibrium. However, as the volume of water increased, this equilibrium was disrupted. Water infiltration progressed, causing the arc length of the meniscus to gradually increase. At this stage, water flow had to surmount interfacial tension. As shown in Fig. 13(c), the pressure difference between the two sides of the curved liquid surface was approximately 20 Pa.

The same process was also observed in N1. As shown in Fig. 13(d), the meniscus was in a contracting process, and the negative pressure difference between the two sides of water-air interface was about 24.4 Pa. In Fig. 13(e), equilibrium was reached. From the pressure isolines at this juncture, it is evident that the isolines on both sides of the meniscus were symmetrically distributed, with equal pressure differences. In Fig. 13(f), the meniscus expanded, requiring water flow to overcome interfacial tension. At this stage, the pressure difference across the water-air interface was approximately 68.7 Pa.

The morphological evolution of the meniscus unfolds in three distinct stages. Initially, during the tension phase, the arc length of the meniscus decreases, propelling water forward as the meniscus contracts. This contraction drives faster water flow. Subsequently, the meniscus reaches an equilibrium state, appearing as a straight line, signifying its arrival at the narrowest pore position. At this point, there is no pressure difference across the interface. Finally, in the expansion phase, the arc length of the meniscus increases as water continues to be injected. With ongoing water injection, interfacial tension escalates while water flow velocity declines. Fig. 14 provides a visual representation of this process, where blue areas denote water, white areas represent air, gray areas indicate particles, and arrows denote the direction of flow at each respective moment.

6. Conclusions

In the present study, experimental and simulation studies were conducted on both heterogeneous and homogeneous

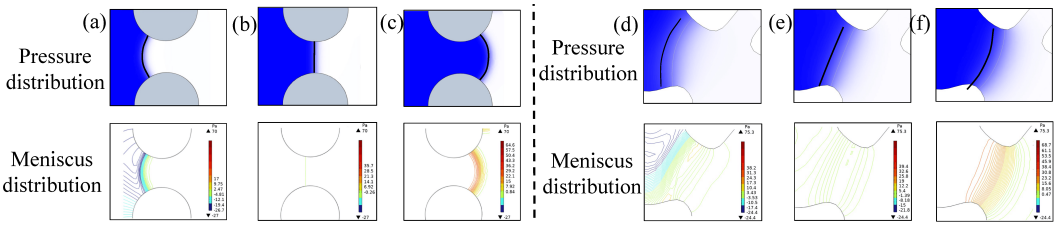

Fig. 13. Meniscus morphology and pressure contour in M4 and N1: (a) Meniscus tension of M4, (b) Meniscus equilibrium of M4, (c) meniscus expansion of M4, (d) meniscus tension of N1, (e) meniscus equilibrium of N1 and (f) meniscus expansion of N1.

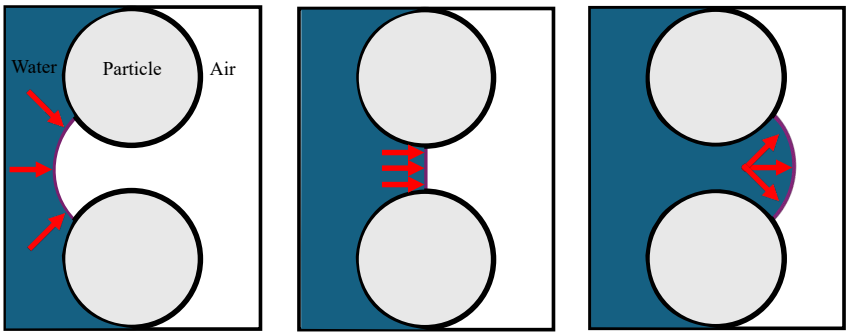

Fig. 14. Schematic diagram of the meniscus motion process.

porous media, maintaining consistent porosity conditions. Through these studies, several conclusions have been drawn.

1) Among homogeneous models, M4 (large pores) exhibits the closest seepage behavior to heterogeneous model N1. Both show similar finger-like flow patterns during infiltration, and their stable water saturation values differ minimally. The saturation curves of both models also display significant fluctuations, reflecting the shared influence of pore scale and connectivity on two-phase flow distribution.
2) Unlike homogeneous media, heterogeneous porous media contain dead-end pores that notably affect water saturation. Air displacement in these dead-end pores is driven by internal-external pressure differences: Water displaces air only when internal pressure surpasses external pressure; otherwise, residual gas accumulates. This unique structural feature explains why heterogeneous media typically have lower water saturation than dense homogeneous media.
3) Water pressure in homogeneous porous media exhibits regular pulse-like fluctuations, with each cycle featuring primary and secondary peaks. As pore size increases, pressure fluctuations become weaker (lower peak values) and slower (longer cycle periods), which is a trend driven by capillary resistance and meniscus dynamics.The queuing effect of water front advancement causes capillary resistance to accumulate, forming primary pressure peaks; the expansion and rupture of menisci between pores further generate secondary peaks.
4) Meniscus evolution during infiltration is governed by pore width changes, following three distinct stages: Tension, equilibrium, and expansion. When moving from wide to narrow pores, the meniscus contracts (driven by interfacial tension); at the narrowest pore section, it reaches equilibrium with no pressure difference across the interface; when transitioning to wide pores, the meniscus expands (requiring water to overcome interfacial tension). This staged evolution directly reflects how pore geometry regulates interfacial forces during seepage.

In conclusion, this study clarifies the regulatory mechanism of pore structure, particularly homogeneity and pore width, on fluid transport in porous media. These findings deepen the understanding of seepage behavior at the pore scale and provide actionable theoretical support for optimizing practical engineering processes such as resource extraction, soil remediation, and CO_2 geological storage.

Acknowledgements

The authors acknowledge the financial support from the Project of Hetao Shenzhen-Hong Kong Science and Technology Innovation Cooperation Zone (No. HZQB-KCZYB-2020083), Shenzhen Science and Technology Program (Nos. KCXFZ20211020163816023 and KCXFZ20230731093901003) and the National Science Foundation of China (No. 5227090113).

Conflicts of interest

The authors declare no competing interest.

Open Access This article is distributed under the terms and conditions of

the Creative Commons Attribution (CC BY-NC-ND) license, which permits unrestricted use, distribution, and reproduction in any medium, provided the original work is properly cited.

References

Adler, P. M., Thovert, J. F. Real porous media: Local geometry and macroscopic properties. Applied Mechanics Reviews, 1998, 51(9): 537-585.

Amiri, H. A., Hamouda, A. A. Pore-scale modeling of non-isothermal two phase flow in 2D porous media: Influences of viscosity, capillarity, wettability and heterogeneity. International Journal of Multiphase Flow, 2014, 61: 14-27.

Bachu, S. Review of CO_2 storage efficiency in deep saline aquifers. International Journal of Greenhouse Gas Control, 2015, 40: 188-202.

Badalassi, V. E., Ceniceros, H. D., Banerjee, S. Computation of multiphase systems with phase field models. Journal of Computational Physics, 2003, 190(2): 371-397.

Cahn, J. W., Hilliard, J. E. Free energy of a nonuniform system. I. Interfacial free energy. The Journal of Chemical Physics, 1958, 28(2): 258-267.

Culligan, P. J., Barry, D. A., Parlange, J. Y., et al. Infiltration with controlled air escape. Water Resources Research, 2000, 36(3): 781-785.

Hizir, F. E., Hardt, D. E. Effect of Substrate contact angle on ink transfer in flexographic printing. Paper COMSOL 99 Presented at COMSOL Conference, Boston, Massachusetts, 4-9 December, 2014.

Holtzman, R., Segre, E. Wettability stabilizes fluid invasion into porous media via nonlocal, cooperative pore filling. Physical Review Letters, 2015, 115(16): 164501.

Hu, R., Wan, J., Kim, Y., Tokunaga, T. K. Wettability impact on supercritical CO_2 capillary trapping: Pore-scale visualization and quantification. Water Resources Research, 2017a, 53(8): 6377-6394.

Hu, R., Wan, J., Kim, Y., Tokunaga, T. K. Wettability effects on supercritical CO_2-brine immiscible displacement during drainage: Pore-scale observation and 3D simulation. International Journal of Greenhouse Gas Control, 2017b, 60: 129-139.

Jacqmin, D. Calculation of two-phase Navier-Stokes flows using phase-field modeling. Journal of Computational Physics, 1999, 155(1): 96-127.

Jiang, Z., Wu, K., Couples, G. D., et al. The impact of pore size and pore connectivity on single-phase fluid flow in porous media. Advanced Engineering Materials, 2011, 13(3): 208-215.

Li, G., Zhan, L., Hu, Z., et al. Effects of particle gradation and geometry on the pore characteristics and water retention curves of granular soils: A combined DEM and PNM investigation. Granular Matter, 2021, 23: 1-16.

Li, G., Zhan, L., Chen, Y., et al. Effects of flow rate and pore size variability on capillary barrier effects: A microfluidic investigation. Canadian Geotechnical Journal, 2022, 60(6): 902-916.

Li, G., Zhan, L., Zhang, Z., et al. Pore network modeling of capillary barrier effects: Impact of pore sizes. Canadian Geotechnical Journal, 2023, 61(1): 174-182.

Lu, Z., Zeng, C., Zhang, Y., et al. Study of the pore size influence on infiltration of porous media considering capillary effect. Capillarity, 2025a, 14(1): 1-12.

Lu, Z., Wang, L., Guo, Z., et al. The microfluidic in geo-energy resources: Current advances and future perspectives. Advances in Geo-Energy Research, 2025b, 16(2): 171-180.

Morrow, N. R., Mason, G. Recovery of oil by spontaneous imbibition. Current Opinion in Colloid & Interface Science, 2001, 6(4): 321-337.

Nimmo, J. R. Porosity and pore size distribution. Encyclopedia of Soils in the Environment, 2004, 3(1): 295-303.

Qin, R. S., Bhadeshia, H. K. Phase field method. Materials Science and Technology, 2010, 26(7): 803-811.

Rokhforouz, M. R., Akhlaghi Amiri, H. A. Phase-field simulation of counter-current spontaneous imbibition in a fractured heterogeneous porous medium. Physics of Fluids, 2017, 29(6): 062104.

Rücker, M., Bartels, W. B., Singh, K., et al. The effect of mixed wettability on pore-scale flow regimes based on a flooding experiment in Ketton limestone. Geophysical Research Letters, 2019, 46(6): 3225-3234.

Sirivithayapakorn, S., Keller, A. Transport of colloids in saturated porous media: A pore-scale observation of the size exclusion effect and colloid acceleration. Water Resources Research, 2003, 39(4): 1109-1121.

Soltanmohammadi, R., Iraji, S., De Almeida, T. R., et al. Insights into multi-phase flow pattern characteristics and petrophysical properties in heterogeneous porous media. Paper EAGE 4609 Presented at Second EAGE Conference on Pre-Salt Reservoir, virtual conference, 8-10 September, 2021.

Soltanmohammadi, R., Iraji, S., de Almeida, T. R., et al. Investigation of pore geometry influence on fluid flow in heterogeneous porous media: A pore-scale study. Energy Geoscience, 2024, 5(1): 100222.

Takada, N., Misawa, M., Tomiyama, A. A phase-field method for interface-tracking simulation of two-phase flows. Mathematics and Computers in Simulation, 2006, 72(2-6): 220-226.

Yong, Y., Lou, X., Li, S., et al. Direct simulation of the influence of the pore structure on the diffusion process in porous media. Computers & Mathematics with Applications, 2014, 67(2): 412-423.

Zalc, J. M., Reyes, S. C., Iglesia, E. Monte-Carlo simulations of surface and gas phase diffusion in complex porous structures. Chemical Engineering Science, 2003, 58(20): 4605-4617.

Zeng, C., Zhang, Y., Lu, H., et al. Simulation of CO_2-water two-phase fluid displacement characteristics based on the phase field method. Deep Underground Science and Engineering, 2025, 4(4): 725-738.

Zhan, L. T., Li, G. Y., Bate, B., et al. A preliminary exploration of the micro-scale behaviour of capillary barrier effect using microfluidics. Géotechnique, 2021, 73(6): 553-560.